An Optimization of the Icosahedral Grid Modified by Spring Dynamics

Hirofumi Tomita,* Masaki Satoh,* and Koji Goto†

*Frontier Research System for Global Change, Integrated Modeling Research Program, 3173-25 Showamachi, Kanazawa-ku, Yokohama-city, Kanagawa, 236-0001, Japan; and †NEC, Scientific Software Department, Supercomputers Marketing Promotion Division 1-10, Nisshincho, Fuchu-city, Tokyo, 183-8501, Japan
E-mail: htomita@jamstec.go.jp

We have investigated an optimum form of the modified icosahedral grid that is generated by applying the spring dynamics to the standard icosahedral grid system. The spring dynamics can generate a more homogeneous grid system than the standard icosahedral grid system by tuning the natural spring lenght: as the natural spring length becomes longer, the ratio of maximum grid interval to minimum one becomes closer to unit. When the natural spring length is larger than a critical value, however, the spring dynamic system does not have a stable equilibrium. By setting the natural spring length to be the marginally critical value, we can obtain the most homogeneous grid system, which is most efficient in terms of the CFL condition. We have analyzed eigenmodes involved in the initial error of the geostrophic balance problem [test case 2 of D. L. Williamson *et al.* (1992, *J. Comput. Phys.* **102**, 211)]. Since the balance state in the discrete system differs slightly from the exact solution of the analytic system, the initial error field includes both the gravity wave mode and the Rossby wave mode. As the results of the analysis are based on Hough harmonics decompositions, we detected Rossby and gravity wave modes with zonal wavenumber 5, which are asymmetric against the equator. These errors are associated with icosahedral grid structure. The symmetric gravity wave mode with zonal wavenumber 0 also appears in the error field. To clarify the evolution of Rossby waves, we introduce divergence damping to reduce the gravity wave mode. From the simulated results of the geostrophic problem with various grid systems, we found that the spuriously generated Rossby wave mode is eliminated most effectively when the most homogeneously distributed grid system is used. It is therefore, concluded that the most homogeneous grid system is the best choice from the viewpoint of numerical accuracy as well as computational efficiency. © 2002 Elsevier Science (USA)

Key Words: shallow water model; icosahedral grid; spring dynamics; climate model.

1. INTRODUCTION

Global climate research requires faster and more accurate solutions of the geophysical dynamics on the spherical geometry. The spectral transform method based on spherical harmonics has been used to solve the dynamical part in the atmospheric GCM (general circulation model) because of its high accuracy. The computational cost of the spectral transform method, however, becomes extremely high as the resolution increases: the computational operations are $O(n^3)$ complex, where n is the truncation number. This is because of the lack of an algorithm for fast Legendre transformation comparable to FFT (fast fourier transformation), although alternative approaches such as the double FFT are being developed [1, 2]. In addition, on massively parallel computers with distributed memories, the spectral transform method has a serious problem: the spectral transform method requires extensive data transfer between computer nodes. For these reasons, it is widely believed that the next generation atmospheric GCM should employ grid method rather than the spectral transform method.

One may employ the simple latitude–longitude grid system as the grid method. However, the latitude–longitude grid method also has another computational problem at high resolutions. In this grid system, the grid spacing near the poles becomes very small as the resolution becomes higher. This causes a very severe limitation on the time interval for advection or the wave-propagation problem to satisfy the CFL (Courant–Friedrich–Lewy) condition [3]. We call this problem the pole problem.

The icosahedral grid method [4, 5] is an attractive alternative to the spectral transform method and the simple latitude–longitude gird method. This grid method has advantages over the latitude–longitude grid method, because it avoids the pole problem by the homogeneity of grid interval. In addition, it has a relatively low computational cost against the spectral transform method at high resolutions. Thus, the icosahedral grid method has high potential for the next generation GCM. Actually, the icosahedral grid has been adopted in a recent climate model [6] and a numerical weather prediction mode [7, 8].

Following Sadourny *et al.* [4] and Williamson [5], who proposed the use of icosahedron as a starting frame for grid generation, many researchers have developed geophysical models using this idea: the barotropic equation models [4, 5, 9], the shallow water equations models [10–15], and the primitive equations models [6–8, 16–18]. In general, finer grid systems are constructed by the recursive division technique as follows. Each side of the original icosahedron whose vertices are on a sphere is projected onto the surface of the sphere. By connecting the midpoints of the geodesic arcs, four subtriangles are generated from each of the spherical triangles. By iterating this procedure, the grid refinement proceeds.

This recursive grid generation method is straightforward. However, in terms of the numerical accuracy, there exists a problem with the combination with the spatial discretization. Heikes and Randall [12] modified the grid system by twisting the icosahedral grid after the first division to obtain the geometrical symmetry against the equator. After the completion of refinement, they further modified the grid system to minimize the error of numerical differential operators [13]. Tomita *et al.* [19] proposed another grid modification by two processes after generating the grid system by the recursive technique. In the first process, neighboring grid points are connected by springs with dampers. Under an appropriate initial condition, grid points are moved until the spring dynamical system calms down to equilibrium. The obtained grid system by this modification dramatically reduces the grid

noise in the integration of the shallow water equations. We call this modified grid system *the spring grid system*. In the second process, the grid points thus determined are moved to the gravitational centers of control volumes. This modification guarantees the second-order accuracy of numerical differential operators at all the grid points. We call this modification *the gravitational-centered relocation*. In the previous paper [19], the authors showed the advantage of the spring grid system with gravitational-centered relocation over the standard grid system by performing the standard test suites of the shallow water equations [20].

Although the modified icosahedral gird system used in [19] provides high numerical accuracy, there is a disadvantage in terms of the computational efficiency; that is, the ratio of the maximum grid interval to the minimum one in the spring grid system is slightly larger than that in the standard grid system. It is a side effect of the application of the spring dynamics.

The main purpose of this paper is to optimize the spring grid system from the viewpoints of both computational efficiency and numerical accuracy. We may say from the former viewpoint that the best grid system is one in which the ratio of the maximum grid interval to the minimum one is closest to unit; if this grid system is used, we can choose the largest time interval that satisfies the CFL condition. However, whether this grid system has the best numerical accuracy remains to be determined. To examine the numerical accuracy, we investigate the evolution of initial error in detail using a series of spring grid system. Based on these results, we conclude that the most homogeneously distributed grid system has the best performance of the numerical accuracy.

The structure of this paper is as follows. In Section 2, grid modification using the spring dynamics is described. Although the spring dynamics was formulated in the previous paper [19], we derive it again in more detail for the sake of subsequent discussion. We also discuss the characteristics of grid systems obtained using the spring dynamics and varying the natural spring length as a parameter. In Section 3, the governing equations and our numerical scheme are described. The analysis method of error field based on the Hough harmonics decomposition is also described. In Section 4, we perform the zonal geostrophic flow problem, which is similar to test case 2 in the standard test suite [20]. The main purpose of this section is a detailed analysis of errors that lie on the icosahedral grid system. Finally, a discussion based on the analysis of the best grid system and concluding remarks are given in Section 5.

2. GRID CONSTRUCTION

2.1. Generation by Spring Dynamics

In this section, we describe generation of the grid system with spring dynamics. Prior to the application of the spring dynamics, we need to construct the standard grid system, which is refined by the same procedure as that of Stuhne and Peltier [9, 14], that is, the recursive division technique. In this paper, the grid resolution obtained by mth dividing operations is called "glevel-m."

The grid location is modified in the following manner. We assume that each grid point has a mass M and that neighboring two grid points are connected by a spring with spring constant k as shown in Fig. 1. We also introduce a damping force to obtain an equilibrium solution. The damping force is proportional to the velocity of motion of the grid point with
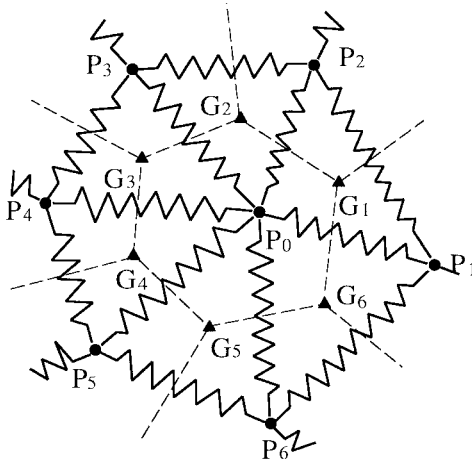
FIG. 1. Schematic figure of spring dynamics on a grid system.

a damping coefficient α. The equation of motion of mass at the point P_0 is described as

$$M\frac{d\mathbf{w}_0}{dt} = \sum_{i=1}^{n} k(d_i - \bar{d})\mathbf{e}_i - \alpha\mathbf{w}_0, \tag{1}$$

$$\frac{d\mathbf{r}_0}{dt} = \mathbf{w}_0, \tag{2}$$

where d_i and $\bar{d}$ are the length of are $P_0 P_i$ and the natural spring length, respectively, $\mathbf{e}_i$ is the unit vector in the direction from P_0 to P_i on the tangential plain at P_0, $\mathbf{w}_0$ is the velocity vector at P_0, $\mathbf{r}_0$ is the position vector of P_0, and n is the number of surrounding mass points interacting with the mass point P_0. In the icosahedral grid configuration, n equals 6 except for the 12 singular points, where n equals 5. When the dynamical system calms down to a static balance with $\mathbf{w}_0 = 0$ and $d\mathbf{w}_0/dt = 0$, the following relation is satisfied:

$$\sum_{i=1}^{n} (d_i - \bar{d})\mathbf{e}_i = 0. \tag{3}$$

Thus, the grid configuration depends only on the tuning parameter $\bar{d}$.

The parameter $\bar{d}$ should be related to a characteristic length of grid interval, which is expressed using the grid division level m as

$$\lambda = \frac{2\pi a}{10 \times 2^{m-1}}, \tag{4}$$

where a is the radius of sphere; λ represents a mean distance between neighboring grid points since the numerator and denominator on R.H.S. in Eq. (4) are the length of the equator and the number of grid points on the equator, respectively. We choose $\bar{d}$ in the form

$$\bar{d} = \beta\lambda, \tag{5}$$

where β is a nondimensional parameter. We use β instead of $\bar{d}$ as the tuning parameter.

Starting from an initial condition of grid points, Eqs. (1) and (2) are numerically solved until the following criterion is satisfied at all the grid points,

$$\left| \sum_{i=1}^{n} (d_i - \bar{d}) \mathbf{e}_i \right| \Big/ \lambda < \epsilon, \tag{6}$$

where ϵ is a small nondimensional number. In all the calculations in this study, we set $\epsilon = 1.0 \times 10^{-4}$. We do not need to use high-order temporal schemes to solve Eqs. (1) and (2), because our interest is only in the stationary state. We use the Euler method as the temporal scheme. After the stationary state is obtained, a control volume at each grid point is defined as a hexagon $G_1 - G_6$ as shown in Fig. 1 by connecting the gravitational centers of triangular elements. Note that the shape of hexagonal control volumes is not a perfect hexagon. However, the control volumes corresponding to the vertices of the original icosahedron are perfect pentagons. Finally, the gravitational-centered relocation [19] is applied to all the grid points: the grid points are moved to the gravitational centers of control volumes. This modification is necessary to guarantee the second-order accuracy of our numerical differential operators, which are described in the next section. Its mathematical proof is given in our previous paper [19]. Furthermore, it is important to note that the gravitational-centered relocation does not change the shape and the size of control volumes, but changes only the location of grid points. In the previous paper [19], this grid system was called the *SPR-GC* grid, and the grid system modified only by the gravitational-centered relocation was called the *STD-GC* grid. In this paper, omitting the symbol *GC* for simplicity, we call these grid systems the *SPR* grid and the *STD* grid, respectively.

We construct grid systems for glevel-5, 6, and 7 with increasing β from 0.0 to 1.2. The initial condition for each β is given in a way similar to the multigrid technique as follows. First, the *STD* grid with glevel-5 is used as the initial condition for the construction of the *SPR* grid with glevel-5. After the *SPR* grid at this resolution for each of βs is obtained by spring dynamics, it is divided only once by the grid division method to obtain an initial condition for glevel-6. We can obtain the *SPR* grid of glevel-6 for each β by solving Eqs. (1) and (2). The initial conditions for glevel-7 are determined in the same manner using the *SPR* grids with glevel-6. In the cases of the higher resolution with glevel-6 and 7, less computational time is required with this method than with a method where the *STD* grid with the same glevel is given as the initial condition. This is because the disturbance of a relatively large wavelength, whose damping time is larger than that of a small wavelength, is eliminated in advance by using the previous equilibrium solution of the coarser resolution. We should note that the 12 vertices of the original icosahedron do not need to be moved because the locations of these points in the initial condition are the same as those in the equilibrium state.

2.2. Characteristics of Grid Systems

Figures 2a and 2b show the structures of glevel-5 grid systems for the *STD* grid and the *SPR* grid with $\beta = 0.4$. Note that this value of β was used in the previous paper [19]. Figures 2a and 2b show that the grid points near the vertices of the original icosahedron in the *SPR* grid are denser than those in the *STD* grid.

As a characteristic length of the grid interval, we define l by root of area of control volume. Figure 3 shows the scatter plot of l against $\sin(\phi)$ for the *STD* grid and the *SPR* grid with $\beta = 0.4$, where ϕ is latitude. The values of l in Fig. 3 are scaled by using the radius of the

(a)

(b)
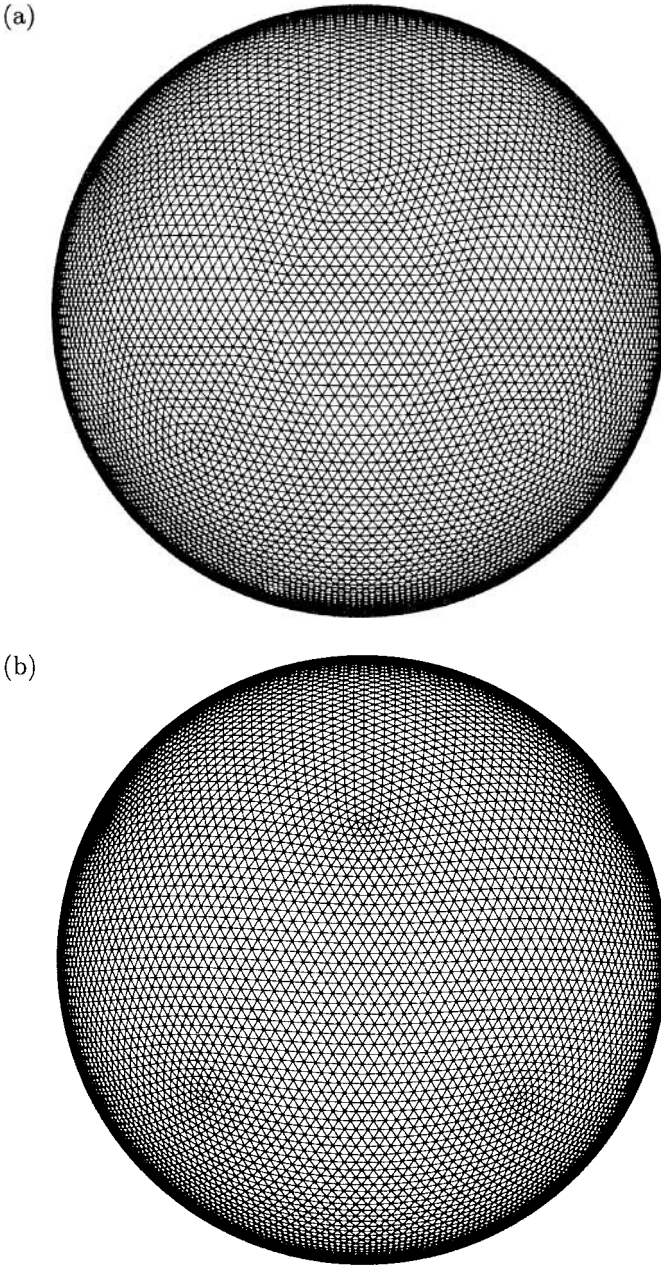
FIG. 2. (a) Grid structure of the *STD* grid with glevel-5. (b) Grid structure of the *SPR* grid ($\beta = 0.4$) with glevel-5. (c) Grid structure of the *SPR* grid ($\beta = 1.2$) with glevel-5.

earth. The maximum value of l, which is indicated at the centers of the major triangles in the original icosahedron, is slightly reduced by a factor of 1.05 with the application of the spring dynamics. On the other hand, the minimum value of l at the singular points is much reduced by a factor of 1.44. Consequently, the ratio of l_{max} to l_{min} becomes higher from 1.34 to 1.82. Thus, the ratio of the maximum grid interval to the minimum one is changed by grid modification by spring dynamics.

The ratio l_{max}/l_{min} in the *SPR* grid depends on both glevel and β. In contrast, the value of l_{max}/l_{min} in the *STD* grid converges to 1.34 as the glevel increases [19]. We call this value

(c)
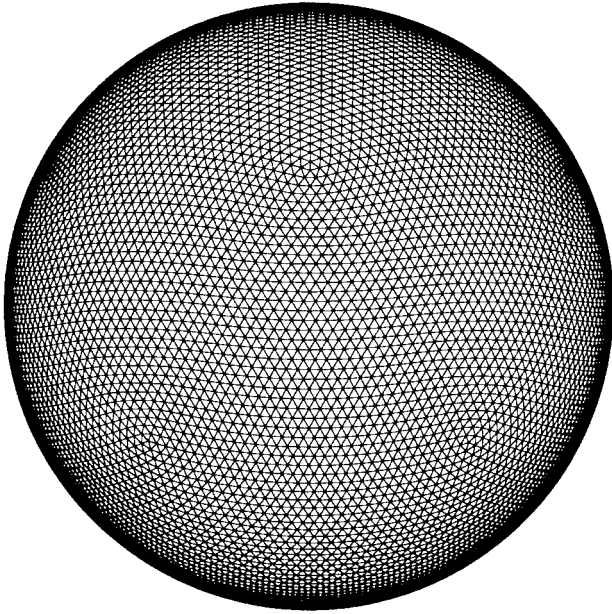
FIG. 2—*Continued*
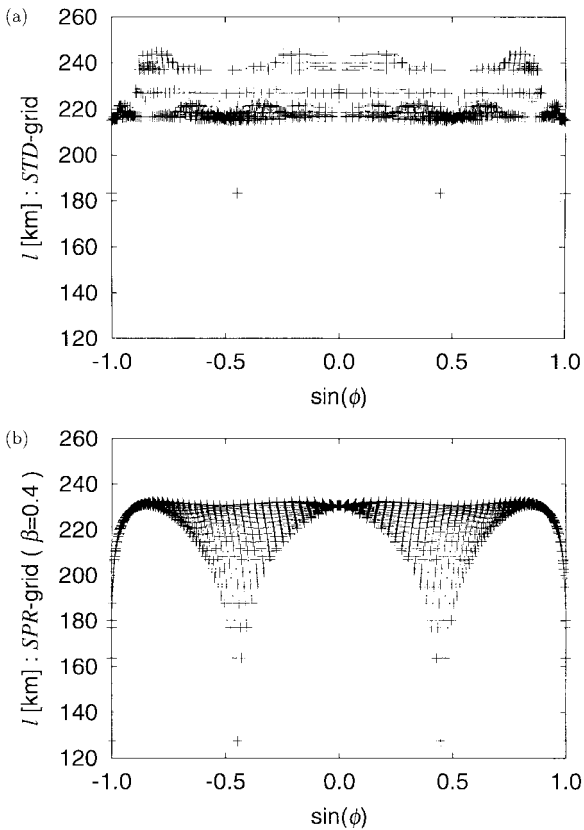
FIG. 3. (a) Scatter plot of l and $\sin(\phi)$ for the *STD* grid with glevel-5, where ϕ is latitude. (b) Scatter plot of l and $\sin(\phi)$ for the *SPR* grid ($\beta = 0.4$) with glevel-5.
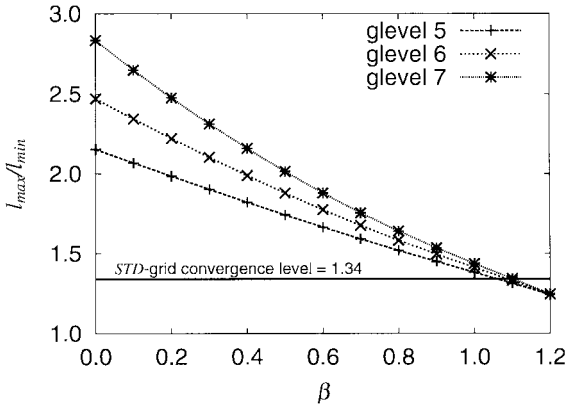
FIG. 4. Dependency of ratio of the maximum grid interval to the minimum one on β and glevel.

the *STD* grid convergence level. Figure 4 shows the plot of l_{max}/l_{min} against β for glevel-5, 6, and 7. The value of l_{max}/l_{min} is reduced as β increases. If $\beta < 1.1$, the value of l_{max}/l_{min} exceeds the *STD* grid convergence level. We can also find that the value of l_{max}/l_{min} at the same β increases as the glevel increases. This tendency intensifies as β becomes smaller.

As shown in Fig. 4, if $\beta = 1.2$, the values of l_{max}/l_{min} for different glevels are almost the same and enough below the *STD* grid convergence level. From the viewpoint of computational efficiency, the value of $\beta = 1.2$ is the best choice of the values used ($0.0 \leq \beta \leq 1.2$), because this configuration provides the most homogeneous grid as shown in Fig. 2c. The numerical accuracy of the shallow water equations using this grid system is discussed in Section 4.

We also investigate the dependency of the shape of control volume on β and glevel. θ_i denotes the angle of control volume at the vertex $G_i (i = 1 \sim 5, 6)$ and the quantity q is defined for each of control volumes as

$$q = \frac{\max(\theta_i)}{\min(\theta_i)} - 1, \tag{7}$$

where max and min denote the maximum and minimum values in six or five vertices of a control volume. Note that the value of q vanishes when the control volume is a perfect hexagon or pentagon.

The maximum value of q in all control volumes is denoted by q_{max}. Figure 5 shows the plot of q_{max} against β for glevel-5, 6, and 7. We find that the value of q_{max} is the *STD* grid converges to 0.14 as the glevel increases. We call this value the *STD* grid convergence level for q_{max}. For each glevel, q_{max} has a minimum value around $\beta = 0.4$. When $\beta > 0.4$, q_{max} increases monotonically and it has a maximum value at $\beta = 1.2$. However, the maximum value is almost the same degree as the *STD* grid convergence level.

If β exceeds the value of 1.2, we find that it is difficult to obtain an equilibrium of the dynamical system. Actually, monitoring the maximum value of the left-hand side of Eq. (6), it becomes oscillatory in time. This fact can be explained as follows. The sum of all the potential energy of the springs has a minimum value when the spring system is in the equilibrium state. In addition, any *local* system that is defined as six or five springs around a given mass point must be in stable equilibrium; that is, the sum of potential energy of these springs around the mass point should be minimum. If β is sufficiently small, all of the
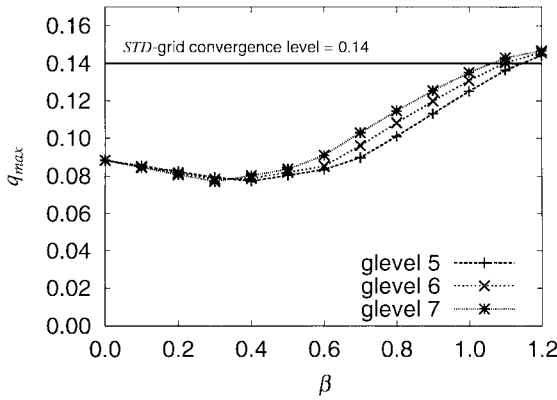
FIG. 5. Dependency of q_{max} on β and glevel.

local potential energy is minimum at the equilibrium state, where all of the spring tensions are positive. If β becomes larger, some of the spring tensions might be negative so that the equilibrium state is unstable.

Let us consider a simple local system that contains six springs on a flat plane. One end of the spring is connected at a mass point (x, y) and the other end is fixed on the unit circle at

$$\begin{pmatrix} x_k \\ y_k \end{pmatrix} = \begin{pmatrix} \cos(n\pi/3) \\ \sin(n\pi/3) \end{pmatrix} \quad n = 1, 2, \ldots, 6. \tag{8}$$

In this situation, any length between neighboring mass points equals to unit. We define the natural spring lenght by β'. The potential energy of this system is written as a function of the location of the mass point (x, y):

$$PE(x, y) = \frac{1}{2}k \sum_{i=1}^{6}(\sqrt{(x - x_k)^2 + (y - y_k)^2} - \beta')^2. \tag{9}$$

Figure 6 shows the distributions of PE for different values of β'. When β' is small (Figs. 6a and 6b), the origin is the unique minimum of PE and thus the equilibrium state is stable. If β' becomes large and exceeds a critical value ($\simeq 1.5$), six other minimum points of PE appear around the unit circle (Fig. 6c). Although the equilibrium state at the origin is still stable, it becomes difficult for the spring dynamics to find the minimum of PE at the origin (Fig. 6d). When β' is at another critical value ($\simeq 2.0$), the equilibrium state at the origin is neutral (Fig. 6e). If β' exceeds the second critical value, the origin is not a minimum point of PE but a maximum point and thus the equilibrium at the origin is unstable (Fig. 6f).

Focusing again on the grid generation, the spring dynamics with $\beta = 1.2$ converges to a balance state, so that all local systems in the *SPR* grid system with $\beta = 1.2$ should be stable as shown in Fig. 6b or 6c. On the other hand, for β higher than 1.2, several local spring dynamics cannot find the minimum of PE at the center of hexagon as shown in Fig. 6d or the centers themselves are unstable as shown in Fig. 6f.

(a) $\beta' = 0.25$
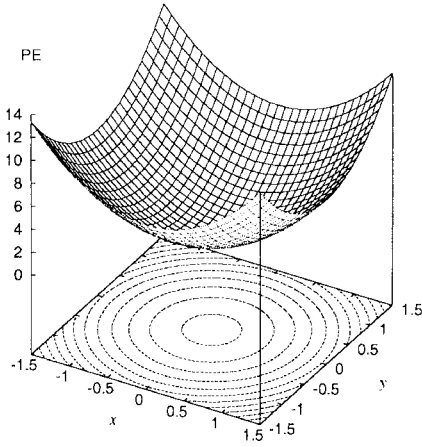
(b) $\beta' = 1.0$
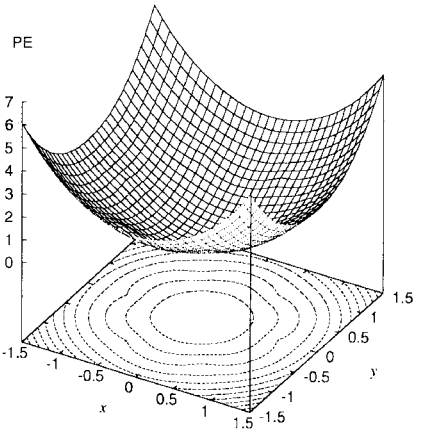
(c) $\beta' = 1.5$
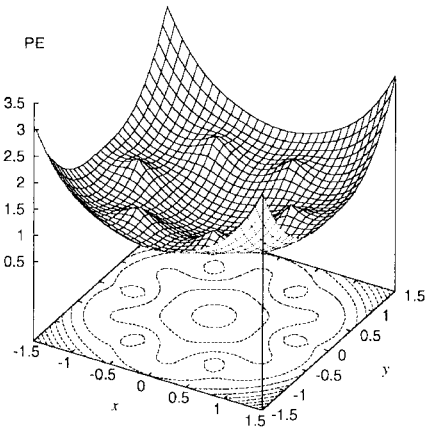
(d) $\beta' = 1.75$
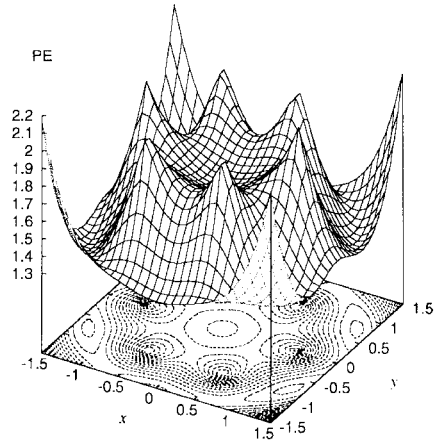
(e) $\beta' = 2.0$
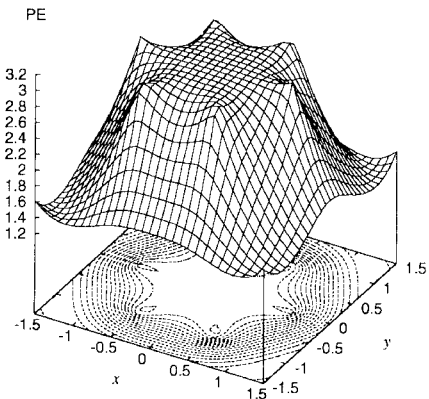
(f) $\beta' = 2.5$
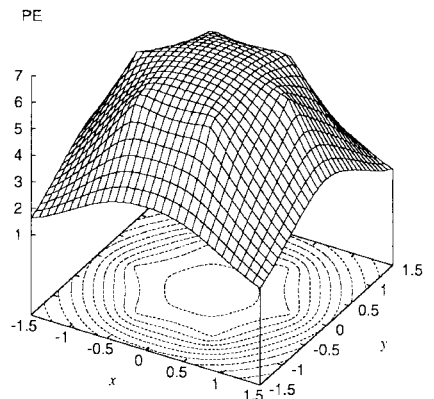
FIG. 6. Potential energy distribution of a local spring system.

3. NUMERICAL METHOD

3.1. Shallow Water Equations and Numerical Scheme

The shallow water equations not only are suitable for the performance test of a grid system but also are a first step in global three-dimensional general circulation models of both atmosphere and ocean, because they contain fundamental phenomena in the meteorological field, e.g., the gravity wave and the Rossby wave.

The shallow water equations on the spherical geometry are described in the vector invarient form as

$$\frac{\partial \mathbf{v}}{\partial t} + (\xi \zeta + f)\hat{\mathbf{k}} \times \mathbf{v} = -\nabla\left(gh + \xi\frac{\mathbf{v} \cdot \mathbf{v}}{2}\right), \tag{10}$$

$$\frac{\partial h}{\partial t} + \nabla \cdot ((\bar{h} + \xi h')\mathbf{v}) = 0, \tag{11}$$

where $\mathbf{v}$ denotes the velocity vector that lies on the tangential plane on the sphere; h and $\bar{h}$ denote the surface height and the mean fluid depth, respectively; h' is the difference of the surface height from $\bar{h}$; t is time; ∇ is the gradient operator; $\hat{\mathbf{k}}$ is the unit vector in the radial direction; f and g are the Coriolis parameter and the gravitational acceleration; ζ denotes the vertical vorticity defined as

$$\zeta = \hat{\mathbf{k}} \cdot (\nabla \times \mathbf{v}). \tag{12}$$

We introduce the nonlinear flag ξ, which equals 1 for the nonlinear system and 0 for the linear system.

The gradient operator in Eq. (10), the divergence operator in Eq. (11), and the curl operator in Eq. (12) are discretized by the finite volume method. The discretization of these operators is the same as that in our previous paper [19]. Here, we review them for the sake of discussion. If a set of vectors $\mathbf{u}$ is given at all the vertices of triangles P_i in Fig. 1, vectors $\mathbf{u}$ at the vertices of control volume G_i are interpolated as

$$\mathbf{u}(G_i) \simeq \frac{\alpha\mathbf{u}(P_0) + \beta\mathbf{u}(P_i) + \gamma\mathbf{u}\left(P_{1+mod(i,6)}\right)}{\alpha + \beta + \gamma}, \tag{13}$$

where α, β, and γ are the areas of $G_i P_i P_{1+mod(i,6)}$, $G_i P_{1+mod(i,6)} P_0$, and $G_i P_0 P_i$, respectively. The number 6 is replaced with 5 in the case of pentagonal control volumes. The divergence and curl operators are calculated from the Gauss theorem as

$$\nabla \cdot \mathbf{u}(P_0) \simeq \frac{1}{A(P_0)} \sum_{i=1}^{6} b_i \frac{\mathbf{u}(G_i) + \mathbf{u}\left(G_{1+mod(i,6)}\right)}{2} \cdot \mathbf{n}_i, \tag{14}$$

$$\hat{\mathbf{k}} \cdot \nabla \times \mathbf{u}(P_0) \simeq \frac{1}{A(P_0)} \sum_{i=1}^{6} b_i \frac{\mathbf{u}(G_i) + \mathbf{u}\left(G_{1+mod(i,6)}\right)}{2} \cdot \mathbf{m}_i, \tag{15}$$

where b_i, $\mathbf{n}_i$, and $\mathbf{m}_i$ denote the geodesic arc length of $G_i G_{1+mod(i,6)}$, the outward unit vector normal to this arc at the midpoint of $G_i G_{1+mod(i,6)}$, and the counter clockwise unit vector parallel to this arc at the midpoint; $A(P_0)$ is the area of control volume at the point P_0.

The gradient operator to an arbitrary variable q is calculated as

$$\nabla q(P_0) \simeq \frac{1}{A(P_0)} \sum_{i=1}^{6} b_i \frac{q(G_i) + q\left(G_{1+mod(i,6)}\right)}{2} \mathbf{n}_i - \frac{q_0}{A(P_0)} \sum_{i=1}^{6} b_i \mathbf{n}_i, \qquad (16)$$

where $q(G_i)$ is interpolated in a way similar to Eq. (13). The second term of Eq. (16) is the correction term. If this term is omitted, the gradient vector of a homogeneous field does not vanish because of curvature of the spherical surface.

The values of R.H.S. in Eqs. (14)–(16) represent the average values over the control volumes, while the values of L.H.S represent the exact values at the grid point P_0. It is proved that only when the grid points are located at the gravitational centers of control volumes do the differences of R.H.S. and L.H.S. have magnitudes of $\mathcal{O}(\Delta d^2)$, where Δd denotes a typical grid interval [19]. Namely, the combination of our spatial discretization and the gravitational-centered relocation gives the second-order accuracy to numerical differential operators.

All the prognostic equations (10) and (11) are explicitly integrated in time. The temporal scheme is the third-order Runge–Kutta method. Arrangement of the grid system can be independently chosen from the rotational axis of the earth. In this study, we set the rotational axis of the earth to penetrate the spherical surface at two of the opposite vertices of the original icosahedron. In all the simulations, we use glevel-5 grid system (approximately $2° \times 2°$ grids) and set the time interval as $\Delta t = 360$ [s].

3.2. Eigenmodes in the Error Field

Before we investigate the numerical accuracy of different grid systems, we should review fundamental behaviors of errors owing to the discretization. Test case 2 in the standard test suite proposed by Williamson *et al.* [20] is suitable for this purpose. This test case is used to investigate temporal evolution of the numerical errors of the initial state that is given by an analytic steady state in the geostrophic equilibrium. Although the original test case 2 is only for the nonlinear system, we extend this test case also to the linear system. The initial condition of the velocity field represents a solid body rotation and the height field is in the geostrophic balance,

$$\tilde{\mathbf{v}}_e = \hat{\mathbf{i}} u_0 \cos \phi, \qquad (17)$$

$$g\tilde{h}_e = gh_0 - \left(a\Omega u_0 + \xi \frac{u_0^2}{2}\right) \sin^2 \phi, \qquad (18)$$

where the tilde ($\sim$) on $\mathbf{v}$ and h means the balance state and subscript e represents the exact solution in the analytic form; $\hat{\mathbf{i}}$ and Ω denote the longitudinal unit vector and the angular velocity of the earth, respectively; u_0 and h_0 are the velocity at the equator and the reference height. In this paper, these values are the same as those of Williamson *et al.* [20]; that is, $a = 6.37122 \times 10^6$[m], $\Omega = 7.292 \times 10^{-5}$[/s], $g = 9.80616$[m/s^2], $u_0 = 2\pi a/12$[days], and $gh_0 = 2.94 \times 10^4$[m^2/s^2].

Although Eqs. (17) and (18) represent a balance state in the continuous system of Eqs. (10) and (11), these equations do not represent a balance state in the discrete system. Let the spatially discretized equations in the linear system ($\xi = 0$) be described as

$$\frac{\partial}{\partial t}\mathbf{v}_d + f\hat{\mathbf{k}} \times \mathbf{v}_d = -\nabla_d(gh_d), \qquad (19)$$

$$\frac{\partial}{\partial t}h_d + \bar{h}\nabla_d \cdot \mathbf{v}_d = 0, \tag{20}$$

where the subscript d represents the discretization. We may have a balanced field in the discrete system near Eqs. (17) and (18),

$$f\hat{\mathbf{k}} \times \tilde{\mathbf{v}}_d = -\nabla_d(g\tilde{h}_d), \tag{21}$$

$$\nabla_d \cdot \tilde{\mathbf{v}}_d = 0, \tag{22}$$

where $\tilde{\mathbf{v}}_d$ and $\tilde{h}_d$ are the velocity and the surface height of the balance state in the discrete system. It should be noted that the existence of the discrete equation set (21) and (22) is not assured. In addition, the balance field of the discrete system may not be uniquely determined. We define the balance state of the discrete system by a temporally averaged field of the numerically evolving solution of Eqs. (19) and (20). Substituting Eqs. (21) and (22) from Eqs. (19) and (20), we can obtain the governing equations of the difference field from the balance state in the discrete system as

$$\frac{\partial}{\partial t}\delta\mathbf{v}_d + f\hat{\mathbf{k}} \times \delta\mathbf{v}_d = -\nabla_d(g\delta h_d), \tag{23}$$

$$\frac{\partial}{\partial t}\delta h_d + \bar{h}\nabla_d \cdot \delta\mathbf{v}_d = 0, \tag{24}$$

where $\delta\mathbf{v}_d = \mathbf{v}_d - \tilde{\mathbf{v}}_d$ and $\delta h_d = h_d - \tilde{h}_d$. If we use $\tilde{\mathbf{v}}_d$ and $\tilde{h}_d$ in Eqs. (21) and (22) as an initial condition for Eqs. (19) and (20), $\delta\mathbf{v}_d$ and δh_d are always zero during the temporal integration of Eqs. (23) and (24). However, if we use $\tilde{\mathbf{v}}_e$ and $\tilde{h}_e$ in Eqs. (17) and (18) as an initial condition for Eqs. (19) and (20), $\delta\mathbf{v}_d$ and δh_d temporally evolve. We can expect that $\delta\mathbf{v}_d$ and δh_d are governed by the same dynamics as the original linear equations. Thus, they may behave as a combination of the eigenmodes, that is, gravity wave modes and Rossby wave modes.

Theoretically, the eigenmodes in the linear shallow water are expressed as the Hough vector harmonics [21, 22]. Any eigenmode might be spuriously generated owing to the discretization error. We may decompose ($\delta\mathbf{v}_d$ and δh_d) by the Hough vector harmonics. In this paper, we denote each eigenmode by the *error mode*. The amplitude of the error modes can be used as an index of the numerical accuracy of the discretization. The Hough vector harmonics are represented as

$$\mathbf{H}_{l,\alpha}^m(\lambda, \phi) = \sum_{n=m}^{\infty} \left(i A_{l,\alpha,n}^m y_{n,1}^m + B_{l,\alpha,n}^m y_{n,2}^m - C_{l,\alpha,n}^m y_{n,3}^m \right)$$

$$y_{n,1}^m = \begin{pmatrix} \frac{im}{\cos\phi} P_n^m \\ \frac{dP_n^m}{d\phi} \\ 0 \end{pmatrix} \frac{\exp(im\lambda)}{\sqrt{n(n+1)}}, \qquad y_{n,2}^m = \begin{pmatrix} -\frac{dP_n^m}{d\phi} \\ \frac{im}{\cos\phi} P_n^m \\ 0 \end{pmatrix} \frac{\exp(im\lambda)}{\sqrt{n(n+1)}}, \tag{25}$$

$$y_{n,3}^m = \begin{pmatrix} 0 \\ 0 \\ P_n^m \end{pmatrix} \exp(im\lambda),$$

where indices m and l represent the zonal mode and the meridional normal mode, respectively. Index α denotes the kind of mode; an eastward or a westward gravity wave for a

$\alpha = 1$ or 2, and a Rossby wave mode for $\alpha = 3$. $y_{n,j}^m$ ($j = 1 \sim 3$) are the spherical vector harmonics. P_n^m are the normalized associated Legendre functions. The first and second components of $\mathbf{H}_{l,\alpha}^m(\lambda, \phi)$ are the zonal velocity and meridional velocity scaled by $\sqrt{g\bar{h}}$, while the third component is the height scaled by $\bar{h}$. As shown in Eq. (25), the Hough harmonics are expanded as the infinite series of the spherical vector harmonics. The expansion coefficients $(A_{l,\alpha,n}^m, B_{l,\alpha,n}^m, C_{l,\alpha,n}^m)$ accompanied with the eigenfrequency can be calculated by the method of Swaztrauber and Kasahara [22]. Since all of the Hough vector harmonics are orthogonal, the amplitude of $\mathbf{H}_{l,\alpha}^m$ in the error field ($\delta\mathbf{v}_d$ and δh_d) can be calculated as

$$S_{l,\alpha}^m = 2 \times \frac{1}{2\pi} \int_0^{2\pi} \int_{-\pi/2}^{\pi/2} \left(\frac{\delta\mathbf{v}_d \cdot \hat{\mathbf{i}}}{\sqrt{g\bar{h}}}, \frac{\delta\mathbf{v}_d \cdot \hat{\mathbf{j}}}{\sqrt{g\bar{h}}}, \frac{\delta h_d}{\bar{h}} \right) \cdot \left(\mathbf{H}_{l,\alpha}^m \right)^* \cos\phi \, d\phi \, d\lambda, \qquad (26)$$

where $\hat{\mathbf{i}}$ and $\hat{\mathbf{j}}$ are the longitudinal and latitudinal unit vectors. $(\mathbf{H}_{l,\alpha}^m)^*$ is the conjugate transpose of $\mathbf{H}_{l,\alpha}^m$.

4. NUMERICAL EXPERIMENTS

In this section, we solve the shallow water equations on the sphere to compare the numerical accuracy between the different grid systems obtained in Section 2.

4.1. Evolution of the Initial Error

4.1.1. *Gravity Wave Error*

We first perform the irrotational case of the linear system, so that $(\xi, \Omega) = (0, 0)$. The grid system used is the *SPR* grid with $\beta = 0.0$. The reason we choose $\beta = 0.0$ is that this grid system possesses enhanced characteristics of the spring grid modification as shown in Fig. 4, and we can expect to clearly detect error modes due to the grid modification by the spring dynamics. Figure 7 shows the temporal variations of l_2 norms for h and $\mathbf{v}$, which are defined by

$$l_2(x) = \frac{\{I[(x - x_e)^2]\}^{1/2}}{\{I[x_e^2]\}^{1/2}}, \qquad (27)$$

where x represents either h or $\mathbf{v}$; I denotes the globally averaging operator; x_e denotes the exact value of x. We can find from Fig. 7 that l_2 norms for h and $\mathbf{v}$ have periodicity of 1.8×10^4 and 3.6×10^4 s, respectively. In this case, all the frequencies of Rossby wave modes are zero because $\Omega = 0$, while gravity wave modes have nonzero frequencies. Thus, the periodicity of l_2 norms in Fig. 7 is caused by a small amplitude of gravity wave superimposed on the balance state in the discrete system.

To extract the error modes, we construct the error fields ($\delta\mathbf{v}_d$ and δh_d) by the following method. We can regard the temporally averaged field during $0 < t < 1.8 \times 10^5$ s as a balanced state in the discrete system. Figure 8a shows the difference height between the temporally averaged field $\tilde{h}_d$ and the exact solution $\tilde{h}_e$. We produce temporal series of anomaly by subtracting the balance state from each of snapshots and regard them as the error fields ($\delta\mathbf{v}_d$ and δh_d). Figures 8b–8j show the temporal series of anomaly for height
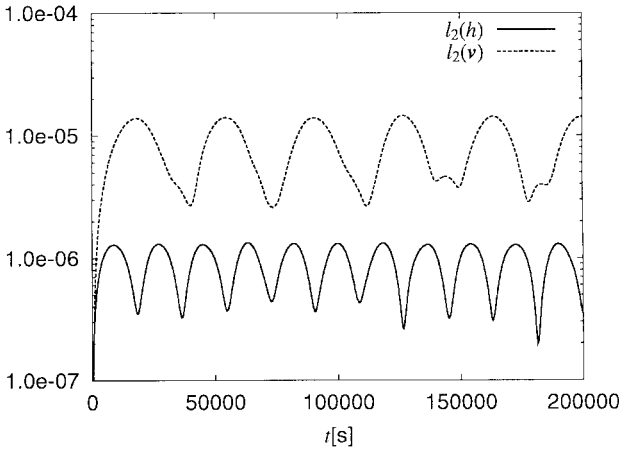
FIG. 7. The temporal variations of l_2 norms for the irrotational linear system using the *SPR* grid ($\beta = 0.0$) with glevel-5.

from $t = 0$ to $t = 3.6 \times 10^4$ s. We can find from Fig. 8 that there is a standing wave with zonal wavenumber 5 that is asymmetric against the equator. The pattern of this error for δh_d is similar to the spherical harmonics Y_6^5.

We analyze the error fields focusing on the wavenumber 5 components by the Hough harmonics deceomposition. Table I shows the periods of gravity wave modes for $l = 0$–5 with respect to $m = 5$ and their amplitudes in the error fields calculated by Eq. (26). For gravity wave modes, an odd value of l represents an asymmetric mode against the equator while an even value of l represents a symmetric mode against the equator. As shown in Table I, amplitudes of $l = 0$, 2, and 4 are extremely small compared with those of $l = 1$, 3, and 5. This fact indicates that the error fields are asymmetric against the equator, corresponding to Fig. 8. Among the asymmetric modes, the mode of $l = 1$ is most dominant. The period of this mode is in good agreement with the period of $l_2(\mathbf{v})$. In addition, the components of eastward gravity waves ($\alpha = 1$) are comparable with those of westward gravity waves ($\alpha = 2$). This fact corresponds to the structure of standing wave. Thus, we can conclude that the error mode of $\mathbf{H}_{1,\alpha=[1,2]}^5$ is the most dominant in this case.

Second, we perform the temporal integration for the case with the rotation of the earth using the linear system. The grid system used is the same as that used in the previous case

TABLE I
Periods and Amplitudes of Gravity Wave Modes for $m = 5$ (the Irrotational Case)

|	$\alpha = 1$		$\alpha = 2$	
	Period (s)	Amplitude	Period (s)	Amplitude
$l = 0$	4.26×10^4	$1.26(\pm0.38) \times 10^{-13}$	-4.26×10^4	$1.26(\pm0.38) \times 10^{-13}$
$l = 1$	3.60×10^4	$5.62(\pm0.18) \times 10^{-6}$	-3.60×10^4	$5.62(\pm0.18) \times 10^{-6}$
$l = 2$	3.12×10^4	$1.29(\pm0.46) \times 10^{-13}$	-3.12×10^4	$1.29(\pm0.45) \times 10^{-13}$
$l = 3$	2.75×10^4	$8.80(\pm3.89) \times 10^{-10}$	-2.75×10^4	$8.80(\pm3.89) \times 10^{-10}$
$l = 4$	2.46×10^4	$6.56(\pm3.09) \times 10^{-14}$	-2.46×10^4	$6.54(\pm3.09) \times 10^{-14}$
$l = 5$	2.23×10^4	$8.27(\pm0.24) \times 10^{-7}$	-2.23×10^4	$8.27(\pm0.24) \times 10^{-7}$

Note. Positive and negative periods represent eastward and westward propagations, respectively. The values in parentheses are the standard deviations during the sampling term.
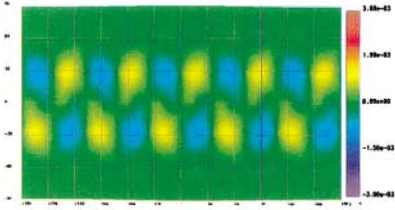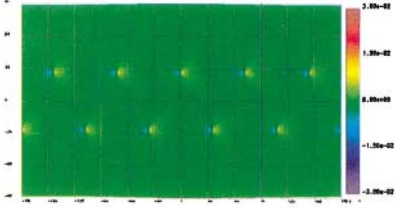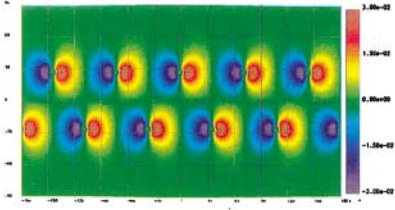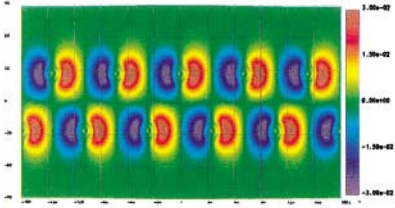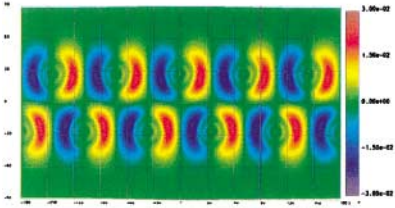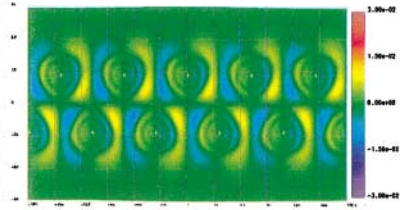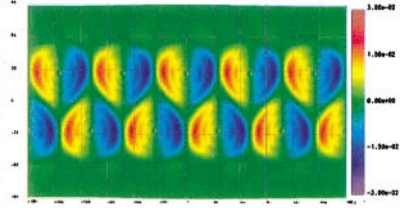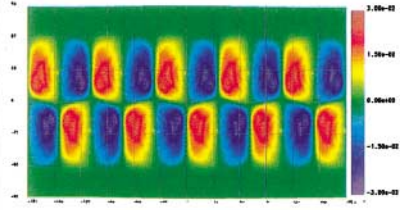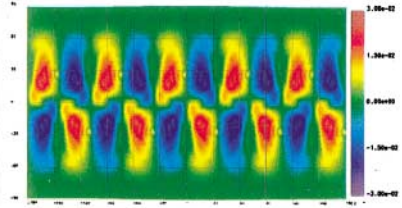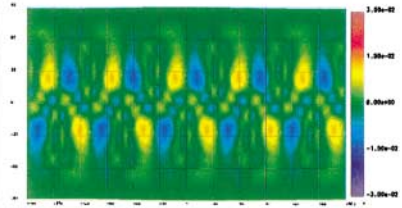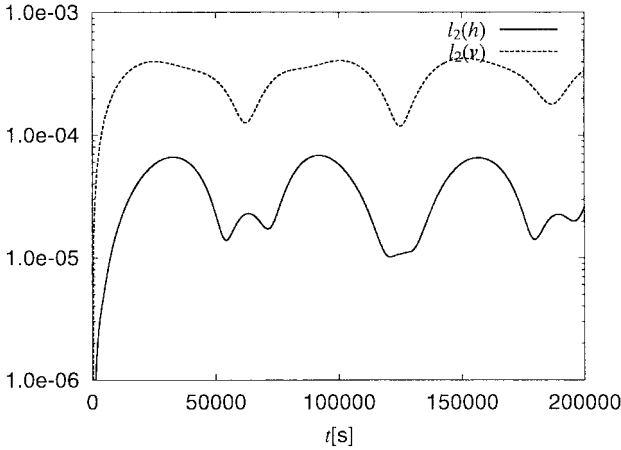
FIG. 8. The temporally averaged field of height error $\tilde{h}_d - \tilde{h}_e$ (a) and the temporal series of anomaly δh_d (b–j) for the irrotational linear case, using the *SPR* grid ($\beta = 0.0$) with glevel-5. $T = 3.6 \times 10^4$ [s].
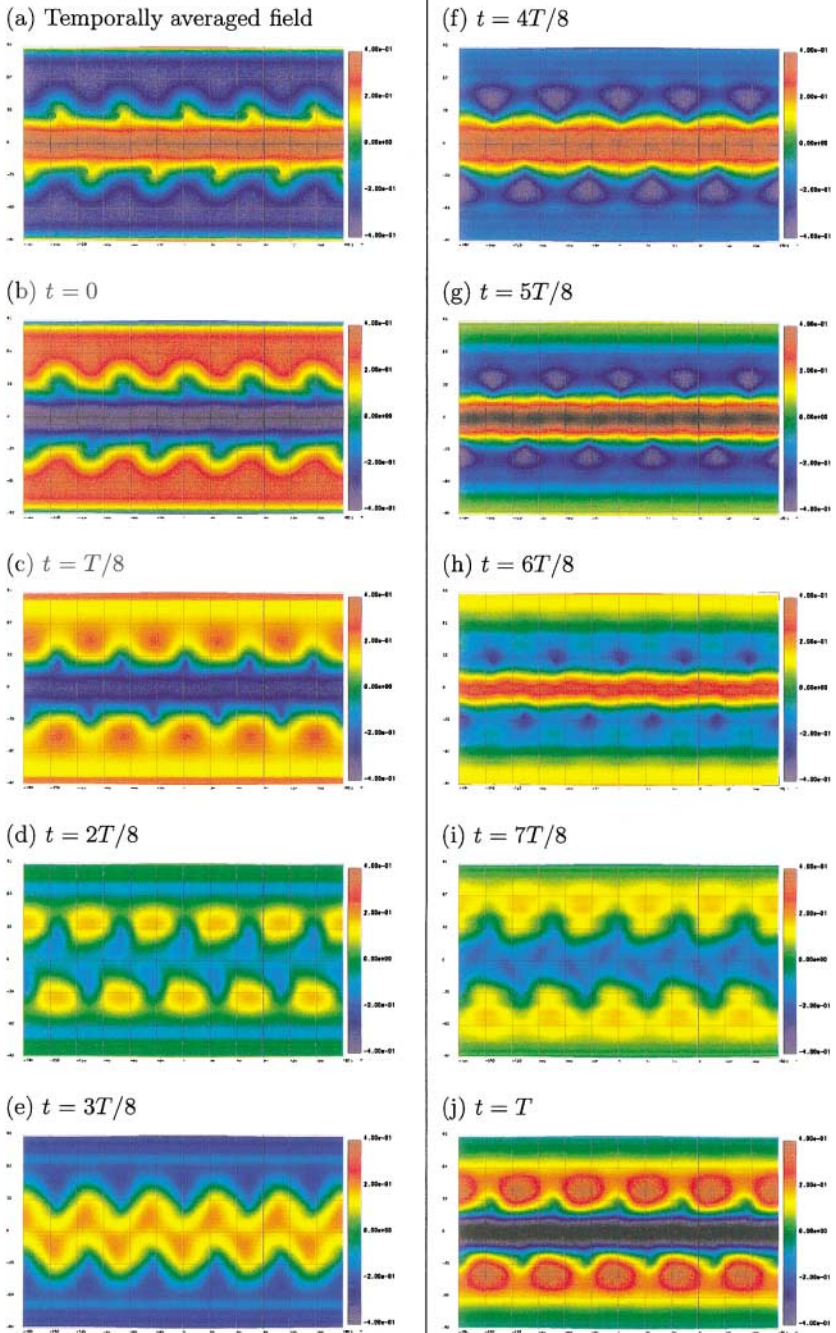
FIG. 10. The temporally averaged field of height error $\tilde{h}_d - \tilde{h}_e$ (a) and the temporal series of anomaly δh_d (b–j) for the rotational linear case, using the *SPR* grid ($\beta = 0.0$) with glevel-5. $T = 6 \times 10^4$ [s].

FIG. 9. The temporal variations of l_2 norms for the rotational linear system, using the *SPR* grid ($\beta = 0.0$) with glevel-5.

($\beta = 0.0$). Figure 9 shows the temporal variations of l_2 norms for h and $\mathbf{v}$. Different from the irrotational case, the dominant period of fluctuation of $l_2(h)$ is the same as that of $l_2(\mathbf{v})$. Although the periodicity is not as clear as the irrotational case, the period T can be estimated as 6×10^4 s from Fig. 9. Figure 10 shows the temporally averaged field $(\tilde{h}_d - \tilde{h}_e)$ from $t = 0$ to $t = 3 \times 10^5$ s and the temporal series of anomaly from $\tilde{h}_d$, which is produced by the same method used in the irrotational case. The dominant wave in this case is a standing wave symmetirc against the equator with meridional node 2 and zonal wavenumber 0. The pattern of this error for δh_d is similar to the spherical harmonics Y_2^0. We can also see that there is a wave with zonal wavenumber 5. However, it seems to be weaker than the wave with zonal wavenumber 0.

Table IIa shows the periods of gravity wave modes for $m = 0$ and their amplitudes in the error fields. The absolute values of two periods of gravity waves ($\alpha = 1, 2$) for each l are the

TABLE II

Periods and Amplitudes of Gravity Wave Modes for $m = 0$ (the Rotational Case)

	$\alpha = 1$		$\alpha = 2$	
	Period (s)	Amplitude	Period (s)	Amplitude
	(a) $m = 0$			
$l = 1$	9.77×10^4	$2.65(\pm1.72) \times 10^{-14}$	-9.77×10^4	$2.65(\pm1.72) \times 10^{-14}$
$l = 2$	5.89×10^4	$2.78(\pm0.14) \times 10^{-4}$	-5.89×10^4	$2.78(\pm0.14) \times 10^{-4}$
$l = 3$	4.67×10^4	$2.55(\pm1.66) \times 10^{-14}$	-4.67×10^4	$2.55(\pm1.66) \times 10^{-14}$
$l = 4$	3.96×10^4	$8.38(\pm1.20) \times 10^{-5}$	-3.96×10^4	$8.38(\pm1.20) \times 10^{-5}$
$l = 5$	3.48×10^4	$2.15(\pm1.35) \times 10^{-14}$	-3.48×10^4	$2.15(\pm1.35) \times 10^{-14}$
$l = 6$	3.11×10^4	$9.25(\pm5.21) \times 10^{-6}$	-3.11×10^4	$9.25(\pm5.21) \times 10^{-6}$
	(b) $m = 5$			
$l = 0$	4.49×10^4	$5.52(\pm2.81) \times 10^{-13}$	-3.80×10^4	$2.60(\pm1.15) \times 10^{-12}$
$l = 1$	3.58×10^4	$1.31(\pm0.038) \times 10^{-5}$	-3.22×10^4	$6.10(\pm0.53) \times 10^{-6}$
$l = 2$	3.03×10^4	$3.18(\pm1.45) \times 10^{-12}$	-2.83×10^4	$9.03(\pm4.07) \times 10^{-13}$
$l = 3$	2.65×10^4	$5.02(\pm0.37) \times 10^{-6}$	-2.53×10^4	$5.19(\pm0.32) \times 10^{-6}$
$l = 4$	2.37×10^4	$1.24(\pm0.60) \times 10^{-12}$	-2.29×10^4	$8.54(\pm3.97) \times 10^{-13}$
$l = 5$	2.15×10^4	$1.28(\pm0.26) \times 10^{-6}$	-2.09×10^4	$9.25(\pm5.21) \times 10^{-6}$

same but their signs are opposite. Since there is no zonal structure for $m = 0$, the amplitudes of eastward and westward gravity waves are also the same. As shown in Table IIa, the amplitudes of even ls are much larger than those of odd ls. The mode $l = 2$ is the most dominant mode for $m = 0$. In addition, the period of the mode $l = 2$ is closest to the period of fluctuation of l_2 norms (6×10^4 [s]). Table IIb shows the periods of gravity wave modes for $m = 5$ and their amplitudes in the error fields. The mode of $l = 1$ and $\alpha = 1$ is the most dominant in the modes of $m = 5$. However, its amplitude is quite smaller than the dominant mode for $m = 0$. Thus, we can conclude that the error field in the rotational case is mostly explained by the gravity wave mode $\mathbf{H}^0_{2,\alpha=[1,2]}$.

4.1.2. Rossby Wave Error

We can expect the existence of Rossby wave modes owing to the initial error. To detect Rossby wave errors clearly, we introduce the divergence damping term into Eq. (10) as

$$\text{L.H.S of (10)} = \text{R.H.S of (10)} + \nu \nabla (\nabla \cdot \mathbf{v}), \tag{28}$$

where ν is the damping coefficient.

Usually, the divergence damping term is introduced in the nonhydrostatic equations to eliminate acoustic waves, which are believed to be less important for the meteorological problems [23]. Since the dynamical mechanics of the gravity wave in the shallow water equations corresponds to that of the acoustic wave in the nonhydrostatic equations, we can effectively filter out the gravity wave mode by the divergence damping term. Although the gravity waves as well as the Rossby waves are important, in the shallow water equations, we dare to use this term only for the current purpose.

Figure 11 shows the temporal variation of $l_2(h)$ in a long-time simulation of the rotational and linear system with divergence damping. The damping coefficient is set as $\nu = 2.5 \times 10^7$ m²/s. The fluctuation of $l_2(h)$ owing to the gravity wave error of $\mathbf{H}^0_{2,\alpha=[1,2]}$ is effectively eliminated by $t = 2.0 \times 10^6$ s. However, another periodicity, which is much longer than that of the gravity wave mode, appears. We can estimate this period T as 5.4×10^5 s. Figure 12 shows the field analysis of height error by the same method as in Figs. 8 and 10. We can find from the temporal series of anomaly (Figs. 12b–12j) that the error distribution is asymmetric
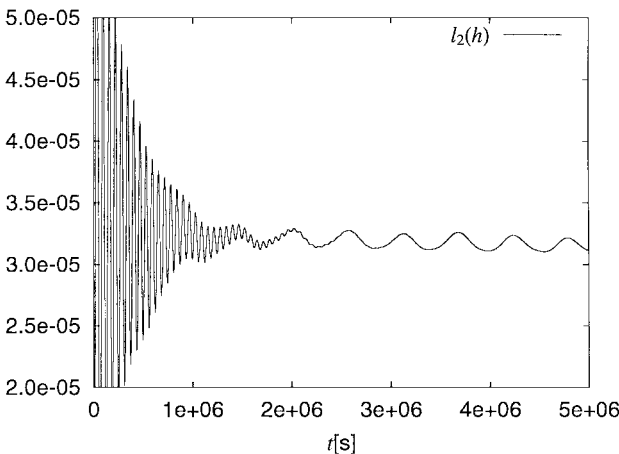
FIG. 11.   Temporal variation of $l_2(h)$ for the rotational linear system with the divergence damping, using the *SPR* grid ($\beta = 0.0$) with glevel-5.
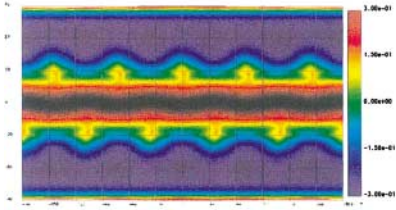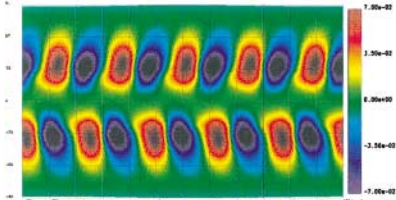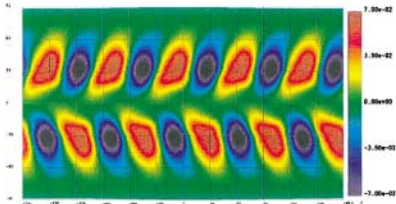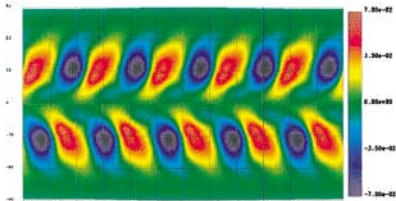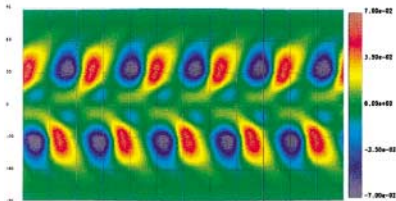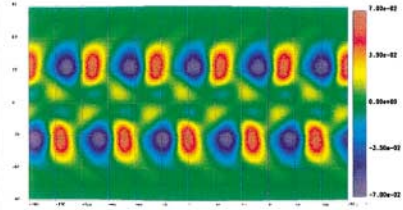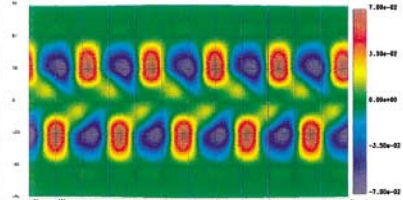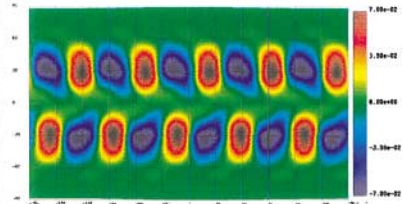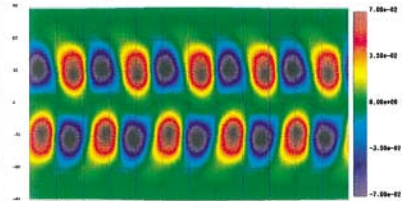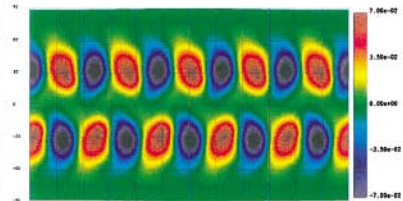
FIG. 12. The temporally averaged field of height error $\tilde{h}_d - \tilde{h}_e$ (a) and the temporal series of anomaly δh_d (b–j) for the rotational linear case with the divergence damping, using the *SPR* grid ($\beta = 0.0$) with glevel-5. $T = 5.4 \times 10^5$ [s].

TABLE III
Periods and Amplitudes of Rossby Wave Modes
for $m = 5$ (the Rotational Case)

	$\alpha = 3$	
	Period (s)	Amplitude
$l = 0$	-2.70×10^5	$3.14(\pm 0.09) \times 10^{-5}$
$l = 1$	-4.08×10^5	$1.21(\pm 0.26) \times 10^{-12}$
$l = 2$	-5.51×10^5	$5.94(\pm 0.21) \times 10^{-5}$
$l = 3$	-7.04×10^5	$2.91(\pm 1.13) \times 10^{-13}$
$l = 4$	-8.70×10^5	$1.15(\pm 0.23) \times 10^{-5}$
$l = 5$	-10.5×10^5	$2.23(\pm 0.95) \times 10^{-13}$

against the equator and with zonal wavenumber 5. Furthermore, the pattern is westward traveling. As shown in Fig. 12a, the temporal averaged field also has a wave with zonal wavenumber 5.

The Rossby wave mode in the linear shallow water equations is expressed as the Hough vector harmonics with $\alpha = 3$ in Eq. (25). Table III shows the periods of the Rossby wave modes for $m = 5$ and amplitudes in the error fields. For the Rossby wave modes, an odd value of l represents a symmetric mode against the equator, while an even value of l represents an asymmetric mode against the equator. (Note that it is contrary to the gravity wave modes.) From Table III, we may say that the mode of $l = 2$ is the primary mode and its period is closest to the period of fluctuation of l_2 norm (5.4×10^5 s). The amplitudes of $l = 0$ and 4 are not negligible, but smaller than that of $l = 2$. Thus, we may say that the error field in this case is almost explained by the Rossby wave mode of $\mathbf{H}^5_{2,\alpha=3}$.

4.2. Comparison of Numerical Accuracy of Spring Grids

In the previous section, we detected the gravity wave error and the Rossby wave error in the linear system. The purpose of this section is to compare the numerical accuracy of the *SPR* grid systems. We perform a long-time simulation of test case 2 in the nonlinear system ($\xi = 1$) using the *SPR* grid systems and varying the value of β. Although the total simulation time is 5 days in the original test case 2 [20], the total simulation time in this study is extended to 60 days in order to detect errors with longer periods. For numerical stability, we add the sixth-order hyperviscosity term to R.H.S. of Eq. (10) as

$$\text{L.H.S of (10)} = \text{R.H.S of (10)} + \mu \nabla^6 \mathbf{v}, \tag{29}$$

where μ is the viscosity coefficient. In this case, we set the coefficient as $\mu = 2.14 \times 10^{26}$ m^6/s so that the e-folding time for waves with two-grid-scale wavelengths is about 30 min.

Figure 13 shows the temporal variations of $l_2(h)$ for $\beta = 0.0, 0.6$, and 1.2. There exist two fluctuations for the case $\beta = 0.0$ as shown in Fig. 13a. One is the fluctuation with a small period estimated as 6×10^4 s and the other is the fluctuation with a large period estimated as 2×10^6 s $\simeq 22$ days. The fluctuation with the small period is owing to the gravity wave mode of $\mathbf{H}^0_{2,\alpha=[1,2]}$ and can be seen also for the cases $\beta = 0.6$ and 1.2 (Figs. 13b and 13c). These results show that the intensity of the gravity wave error is not sensitive to β.

(a) $l_2(h)$: SPR-grid ($\beta=0.0$)

(b) $l_2(h)$: SPR-grid ($\beta=0.6$)

(c) $l_2(h)$: SPR-grid ($\beta=1.2$)
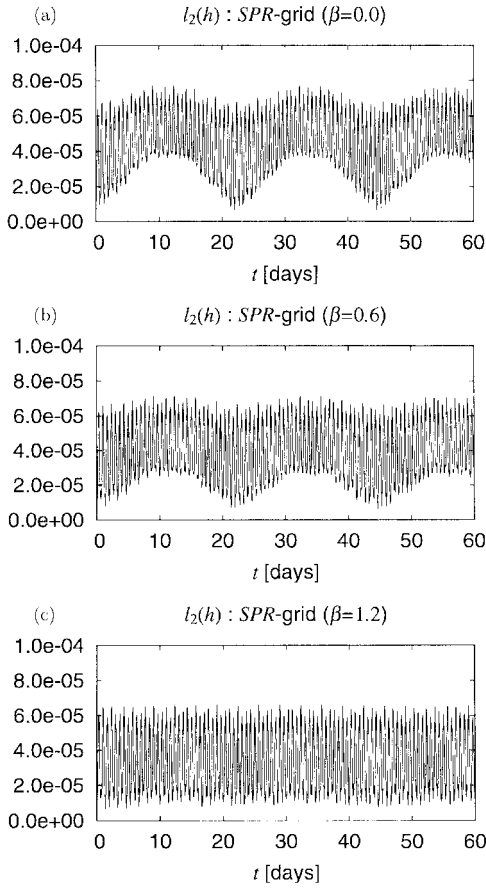
FIG. 13.   The temporal variations of $l_2(h)$ for the nonlinear system.

The fluctuation with the large period corresponds to the Rossby wave mode of $\mathbf{H}^5_{2,\alpha=3}$ in the linear system. However, the period due to this Rossby wave mode is much larger than that of the Rossby wave mode $\mathbf{H}^5_{2,\alpha=3}$ in the linear system. The reason that the period in the nonlinear system becomes larger can be explained as follows. The Rossby wave mode is westward propagating, while the wind due to solid rotation field flows eastward. If c and u denote the phase velocity of the Rossby wave against the medium and the wind velocity, respectively, the westward propagation velocity c_{eff} against the surface can be written as $c_{eff} = c - u$. Thus, the westward propagation velocity is reduced by the wind velocity, so that the period becomes longer. Actually, by the same analysis of the height error as used in the previous subsection, we detected the westward propagation of Rossby wave with a slow speed and obtained the same spatial pattern as shown in Fig. 12.

As shown in Fig. 13, the amplitude with the large period is much reduced if β increases. The amplitude in the case $\beta = 1.2$ is the smallest in three cases. This means that the balance state in the discrete system is much closer to that in the continuous system at the higher β.

To check the performance in a more realistic flow, we also performed test case 5 (zonal flow over an isolated mountain) [20] using the SPR grid systems varying the value of β. In this problem, the gravity waves generated by the initial impact propagate over the sphere during the simulation, so that the dominant error is generated not by the Rossby wave but

by the gravity wave. Consequently, all of the *SPR* grids have the almost same numerical accuracy, because the magnitude of error generated by the gravity wave is not sensitive to β.

5. SUMMARY AND DISCUSSION

In Section 2, we described in detail the grid generation method using spring dynamics, and we generated a set of grid systems by varying the tuning parameter β. The ratio of the maximum grid interval to the minimum one defined by l_{max}/l_{min} becomes smaller and closer to unit as β increases. It is found that the grid hardly converge to any stationary state if β exceeds a critical value around 1.2. We can explain this phenomenon by consideration of the stability of an equilibrium state of a local spring system. If $\beta = 1.2$, the obtained grid is most homogeneous with $l_{max}/l_{min} = 1.24$. This value is smaller than the convergence level(1.34) in the standard grid system. In addition, the dependency of l_{max}/l_{min} on glevel is minimum at $\beta = 1.2$, that is, l_{max}/l_{min} does not vary if the glevel increases. Thus, from the viewpoint of computational efficiency, the *SPR* grid with $\beta = 1.2$ is the best choice.

In Section 4.1, we found that there are two dominant error patterns associated with discretization error in the initial field of the zonal geostrophic problem. One is similar to the spherical harmonics Y_6^5. The other is similar to Y_2^0. These distributions generate error modes, behaviors of which are governed by the original shallow water equations.

The first error Y_6^5 corresponds to the gravity wave mode of the Hough vector harmonics $\mathbf{H}_{1,\alpha=[1,2]}^5$ and the Rossby wave mode $\mathbf{H}_{2,\alpha=3}^5$. This error comes from the icosahedral grid structure, because the grid structure used in this study also has a 5-fold symmetry around the rotational axis and is asymmetric against the equator. Thus, these error modes are peculiar to the icosahedral grid structure.

On the other hand, the second error pattern Y_2^0 corresponds to the gravity wave of $\mathbf{H}_{2,\alpha=[1,2]}^0$. Although the Rossby wave mode due to this error pattern also exists theoretically [22], it cannot be detected because this pattern has no zonal structure. We may say that the error mode of the gravity wave $\mathbf{H}_{2,\alpha=[1,2]}^0$ is free from the symmetry of the grid structure around the rotational axis, because the zonal wavenumber of this mode is zero. Other studies using the icosahedral grid system also show similar fluctuations with this period in l_2 norm for h [9, 12]. Even in the spectral model, there is a fluctuation with the same period (see figure 4.1 in [24]). We can attribute the source of this error to the initial profile; in Eqs. (17) and (18), the meridional distribution of the balance field has a large value at the equator and monotonically decreases toward the poles. The difference in the balance state of the continuous system and that of the discrete system is produced mainly by this meridional distribution. Thus, this error is not peculiar to the icosahedral grid configuration.

Based on the analysis of the evolution of the initial error, we can discuss which value of β produces the best *SPR* grid in terms of the numerical accuracy. As shown in Section 4.2, the magnitude of the gravity wave error is independent of β, while the magnitude of the Rossby wave error becomes smaller as β increases. The Rossby wave error is mostly reduced for the *SPR* grid with $\beta = 1.2$, which is most homogeneous in our grid systems. The Rossby waves as well as the gravity waves are fundamentally important in large-scale dynamics, so that it should be solved as accurately as possible. In this sense, it is desirable that the Rossby wave error should be minimum. Therefore, we conclude that the *SPR* grid with $\beta = 1.2$ is the best choice from the viewpoint of physical performance as well as computational efficiency.

ACKNOWLEDGMENTS

REFERENCES

1. H. Cheong, Double fourier series on a sphere: Applications to elliptic and vorticity equations, *J. Comput. Phys.* **157**, 327 (2000).

2. H. Cheong, Application of double fourier series to the shallow-water equations on a sphere, *J. Comput. Phys.* **165**, 261 (2000).

3. P. J. Roache, *Computational Fluid Dynamics* (Hermora Publishers, 1976).

4. R. Sadourny, A. Arakawa, and Y. Mintz, Integration of the nondivergent barotropic vorticity equation with an icosahedral hexagonal grid for the sphere, *Mon. Wea. Rev.* **96**, 351 (1968).

5. D. L. Williamson, Integration of the barotropic vorticity equation on a spherical geodesic grid, *Tellus* **20**, 642 (1968).

6. T. D. Ringler, R. H. Heikes, and D. A. Randall, Modeling the atmospheric general circulation using a spherical geodesic grid: A new class of dynamical cores, *Mon. Wea. Rev.* **128**, 2471 (2000).

7. D. Majewski, The new global icosahedral-hexagonal gridpoint model GME of the Deutscher Wetterdienst, in proceeding of a seminar held at ECMWF on recent developments in numberical methods for atmospheric modelling, p. 172, Sept. 7–11, 1998.

8. D. Majewski, D. Liermann, P. Prohl, B. Ritter, M. Buchhold, T. Hanisch, G. Paul, and W. Wergen, The operational global icosahedral–hexagonal gridpoint model GME: Description and high-resolution test, *Mon. Wea. Rev.* **130**, 319 (2002).

9. G. R. Stuhne and W. R. Peltier, Vortex erosion and amalgamation in a new model of large scale flow on the shere, *J. Comput. Phys.* **128**, 58 (1996).

10. Y. Masuda and H. Ohnishi, An integration scheme of the primitive equation model with an icosahedral-hexagonal grid system and its application to the shallow water equations, in *Short- and Medium-Range Numerical Weather Prediction: Collection of Papers Presented at the WMO/IUGG NWP Symposium, Tokyo*, p. 317, Aug. 4–8, 1986.

11. M. J. P. Cullen, Integration of the primitive equations on a sphere using the finite element method, *Q. J. R. Met. Soc.* **100**, 555 (1974).

12. R. H. Heikes and D. A. Randall, Numerical integration of the shallow-water equations on a twisted icosahedral grid. I. Basic design and results of tests, *Mon. Wea. Rev.* **123**, 1862 (1995).

13. R. H. Heikes and D. A. Randall, Numerical integration of the shallow-water equations on a twisted icosahedral grid. II. A detailed description of the grid and analysis of numerical accuracy, *Mon. Wea. Rev.* **123**, 1881 (1995).

14. G. R. Stuhne and W. R. Peltier, New icosahedral grid-point discretizations of the shallow water equations on the sphere, *J. Comput. Phys.* **148**, 23 (1999).

15. J. Thuburn, A PV-based-shallow-water model on a hexagonal-icosahedral grid, *Mon. Wea. Rev.* **125**, 2328 (1997).

16. R. Sadourny, Numerical integration of the primitive equations on a spherical grid with hexagonal cells, in *Proceedings of the WMO/IUGG Symposium on Numerical Weather Prediction in Tokyo, Tech. Rep. of JMA*, pp. VII45–VII52, Nov. 26–Dec. 4, 1969.

17. D. L. Williamson, Integration of the primitive barotropic model over a spherical geodesic grid, *Mon. Wea. Rev.* **98**, 512 (1969).

18. M. J. P. Cullen and C. D. Hall, Forecasting and general circulation results from finite element models, *Q. J. R. Met. Soc.* **105**, 571 (1979).

19. H. Tomita, M. Tsugawa, M. Satoh, and K. Goto, Shallow water model on a modified icosahedral geodesic grid by using spring dynamics, *J. Comput. Phys.* **174**, 579–613 (2001).

20. D. L. Williamson, J. B. Drake, J. J. Hack, R. Jacob, and P. N. Swarztrauber, A standard test set for numerical approximations to the shallow water equations in spherical Geometry, *J. Comput. Phys.* Vol. 102, p. 211. 1992.

21. M. S. Longuet-Higgins, The eigenfunctions of Laplace's tidal equations over a sphere, *Phil. Trans. Roy. Soc. London* **A262**, 511 (1968).

22. P. N. Swarztrauber and A. Kasahara, The vector harmonic analysis of Laplace's tidal equations, *SIAM J. Sci. Stat. Comput.* **6**, 464 (1985).

23. W. C. Skamarock and J. Klemp, The stability of time-split numerical method s for the hydrostatic and the nonhydrostatic elastic equations, *Mon. Wea. Rev.* **120**, 2109 (1992).

24. R. Jakob-Chien, J. J. Hack, and D. L. Williamson, Spectral transform solutions to the shallow water test set, *J. Comput. Phys.* **119**, 164 (1995).